Active Contours Driven by Local and Global Intensity Fitting Energy with Application to Brain MR Image Segmentation

Li Wang [a], Chunming Li [b,*], Quansen Sun [a]

Deshen Xia [a], Chiu-Yen Kao [c]

[a] *School of Computer Science & Technology, Nanjing University of Science and Technology, Nanjing, 210094, CHINA*

[b] *Institute of Imaging Science, Vanderbilt University, Nashville, TN 37232-2310, USA*

[c] *Department of Mathematics and Mathematical Biosciences Institute, The Ohio State University, Columbus, OH 43210-1174, USA*

Abstract

In this paper, we propose an improved region-based active contour model in a variational level set formulation. We define an energy functional with a local intensity fitting term, which induces a local force to attract the contour and stops it at object boundaries, and an auxiliary global intensity fitting term, which drives the motion of the contour far away from object boundaries. Therefore, the combination of these two forces allows for flexible initialization of the contours. This energy is then incorporated into a level set formulation with a level set regularization term that is necessary for accurate computation in the corresponding level set method. The proposed model is first presented as a two-phase level set formulation and then extended to a multi-phase formulation. Experimental results show the advantages

Preprint submitted to Computerized Medical Imaging and Graphics13 March 2009

of our method in terms of accuracy and robustness. In particular, our method has been applied to brain MR image segmentation with desirable results.

Key words: Image segmentation; Intensity inhomogeneity; Active contour model; Level set method; Variational method

1 Introduction

Since the introduction by Kass *et al.* [1], active contour models have been widely used in image segmentation with promising results. The models are able to provide smooth and closed contours to recover object boundaries with subpixel accuracy, which is typically not possible in classical methods, such as edge detection and thresholding. The existing active contour models can be categorized into two classes: edge-based models [1–7] and region-based models [8–17].

In general, edge-based models typically use image gradient as an image-based force to attract the contour toward object boundaries. These models have been successfully used for general images with strong object boundaries, but they may suffer from boundary leakage problem for brain MR images, which typically contain weak boundaries between gray matter and white matter due to low contrast and partial volume effect. Region-based models have better performance than edge-based models in the presence of weak boundaries. However, region-based models [8,9,12,10,13,14] tend to rely on intensity homogeneity. For example, the well-known piecewise constant (PC) models [12,10,14]

* Corresponding author.
Email address: chunming.li@vanderbilt.edu (Chunming Li).

are based on the assumption that image intensities are statistically homogeneous in each region, and therefore they fail to segment MR images with intensity inhomogeneity. In [10] and [11], two similar region-based active contour models were proposed for the segmentation of more general images. These models are based on a piecewise smooth description of the images, and thus have been known as piecewise smooth (PS) models. Therefore, the PS models have exhibited certain capability of handling intensity inhomogeneity. The computational cost of the PS models is, however, rather expensive due to the complicated procedures involved [18,17]. This limitation, along with their somewhat complex parameter settings, has made the PS models barely useful for MR brain image segmentation.

In fact, intensity inhomogeneity occurs in many real-world images from different modalities [19,20]. In particular, it is often seen in medical images, such as X-ray radiography/tomography and magnetic resonance (MR) images. For example, the intensity inhomogeneity in MR images often appears as an intensity variation across the image, which arises from radio frequency (RF) coils or acquisition sequences. Thus the resultant intensities of the same tissue vary with the locations in the image. Similar artifacts also occur in CT images due to the beam hardening effect, as well as in ultrasound images caused by non-uniform beam attenuation within the body.

Recently, Li *et al.* proposed a local binary fitting (LBF) model to overcome the difficulty in segmentation caused by intensity inhomogeneity [17,21]. The LBF model draws upon spatially varying local region information and thus is able to deal with intensity inhomogeneity. By using local region information, specifically local intensity mean, the LBF model is able to provide desirable segmentation results even in the presence of intensity inhomogeneity. Some

related methods were recently proposed in [18,22], which have similar capability of handling intensity inhomogeneity as the LBF model. These methods [17,21,18,22] are, however, to some extent sensitive to initialization, which limits their practical applications.

In this paper, we propose an improved region-based active contour model in a variational level set formulation. We define an energy functional [1] with a local intensity fitting term, which is dominant near object boundaries and responsible for attracting the contour toward object boundaries, and an auxiliary global intensity fitting term, which incorporates global image information to improve the robustness of the proposed method. In addition, this energy is then incorporated into a level set formulation with a level set regularization term that is necessary for accurate computation in the corresponding level set method. In the associated curve evolution, the motion of the contour is driven by a local intensity fitting force and a global intensity fitting force, induced by the local and global terms in the proposed energy functional, respectively. The influence of these two forces on the curve evolution is complementary. When the contour is close to object boundaries, the local intensity fitting force becomes dominant, which attracts the contour toward and finally stops the contour at object boundaries. This force plays a key role in accurately locating object boundaries, especially for images with intensity inhomogeneity. The global intensity fitting force is dominant when the contour is far away from object boundaries, and it allows more flexible initialization of contours by using global image information. The proposed model is first presented as a two-phase level set formulation and then extended to a multi-phase formu-

[1] In calculus of variations, an energy functional refers to an energy whose variables are functions (e.g. f_1, f_2, ϕ in our model).

lation for brain MR image segmentation.

Note that part of results in this paper were reported in our recent conference paper [23]. The remainder of this paper is organized as follows. In Section 2, we review some well-known region-based models and their limitations. The proposed method is introduced in Section 3. The implementation and results are given in Section 4, followed by some discussions in Section 5. This paper is summarized in Section 6.

2 Background

2.1 Piecewise constant models

Chan and Vese [12] proposed an active contour approach to the Mumford-Shah problem [24] for a special case where the original image is a piecewise constant function. Let $\Omega \subset \Re^2$ be the image domain, $I : \Omega \rightarrow \Re$ be a given gray level image. The variable $\mathbf{x}$ in $I(\mathbf{x})$ is a point in Ω. They proposed the following energy:

$$\begin{aligned}\mathcal{E}^{\mathrm{CV}}(c_1, c_2, C) = \lambda_1 \int_{outside(C)} |I(\mathbf{x}) - c_1|^2 d\mathbf{x} \\ + \lambda_2 \int_{inside(C)} |I(\mathbf{x}) - c_2|^2 d\mathbf{x} + \nu |C|\end{aligned} \tag{1}$$

where *outside(C)* and *inside(C)* represent the regions outside and inside the contour C, respectively, and c_1, c_2 are two constants that approximate the image intensity in *outside(C)* and *inside(C)*. $|C|$ is the length of the contour C. The parameters λ_1, λ_2 and ν are nonnegative constants. We call the first two terms in (1) the global data fitting energy. One of the most attractive

properties of the CV model is that it is much less sensitive to the initialization.

Such optimal constants c_1 and c_2 can be far different from the original data, if the intensities within *outside(C)* and *inside(C)* are inhomogeneous. Without taking local image information into account, the CV model generally fails to segment images with inhomogeneity. For example, Fig. 1(a) shows a synthetic image with intensity inhomogeneity. The contour is initialized as a circle. The CV model fails to segment this image, as shown in Fig. 1(b). It is clearly seen that some part of the background/foreground is incorrectly identified as the foreground/background. Likewise, more general piecewise constant models in a multi-phase level set framework [10,13,14] are not applicable for such images either.

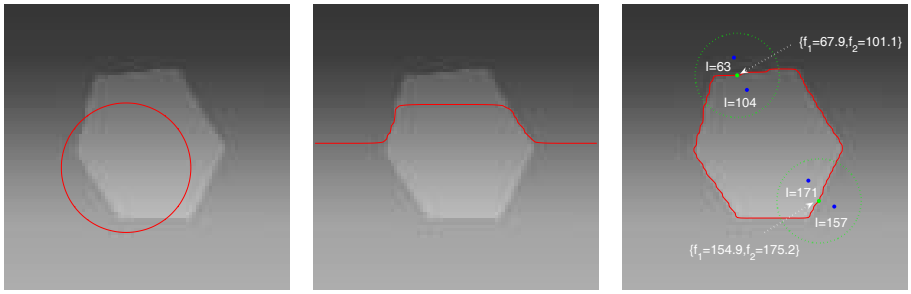

(a) (b) (c)

Fig. 1. Experiments for a synthetic image with intensity inhomogeneity. (a) Original image and initial contour. (b) Result of the CV model. (C) Result of the LBF model, with intensities at four points (shown in blue) and values $\{f_1, f_2\}$ at two points (shown in green) indicated.

2.2 The local binary fitting model

The local binary fitting (LBF) model [17] was recently proposed to segment images with intensity inhomogeneity, utilizing the local intensity information

efficiently, and has achieved promising results. Two fitting functions $f_1(\mathbf{x})$ and $f_2(\mathbf{x})$ that locally approximate the intensities outside and inside the contour are introduced in the LBF model. In contrast to the two constants c_1 and c_2 in the CV model, the functions $f_1(\mathbf{x})$ and $f_2(\mathbf{x})$ are spatially varying fitting functions. They proposed to minimize the following energy

$$\begin{aligned}\mathcal{E}^{\mathrm{LBF}}(C, f_1, f_2) = \lambda_1 \int \Big[\int_{outside(C)} K_\sigma(\mathbf{x}-\mathbf{y})|I(\mathbf{y}) - f_1(\mathbf{x})|^2 d\mathbf{y}\Big] d\mathbf{x} \\ + \lambda_2 \int \Big[\int_{inside(C)} K_\sigma(\mathbf{x}-\mathbf{y})|I(\mathbf{y}) - f_2(\mathbf{x})|^2 d\mathbf{y}\Big] d\mathbf{x} \\ + \nu|C| \end{aligned} \tag{2}$$

where K_σ is a Gaussian kernel with standard deviation σ. The first two terms are the local intensity fitting energy, denoted by $\mathcal{F}^{\mathrm{LBF}}$. This energy can be represented by a level set formulation, and then the energy minimization problem can be converted to solving a level set evolution equation [17].

Due to the localization property of the kernel function, the contribution of the intensity $I(\mathbf{y})$ to the LBF energy decreases to zero as the point $\mathbf{y}$ moves away from the center point $\mathbf{x}$. Therefore, the LBF energy is dominated by the intensity $I(\mathbf{y})$ of points $\mathbf{y}$ in a neighborhood of $\mathbf{x}$. This localization property plays a key role in segmenting the images with intensity inhomogeneity. For example, we apply the LBF model to segment the image shown in Fig. 1(a), which has shown that the CV model fails to segment the object correctly. Fig. 1(c) shows the correct result of the LBF model. It is clearly seen that spatially varying fitting functions f_1 and f_2 approximate the local intensities on the two sides of the contour very well. For example, the values of f_1 and f_2 at the green point in the upper left part of the image are 67.9 and 101.1 respectively, which are consistent with the local intensities.

However, such localization property may introduce many local minimums of the energy functional. Consequently, the result is more dependent on the initialization of contour. This can be seen from a simple experiment for a binary image with a special initial contour as shown in Fig. 2(a). Note that this special initial contour is generated manually. The intensities of the background and foreground are 100 and 150 respectively. Fig. 2(b) shows the final segmentation result of the LBF model. It can be seen that the contour is stuck in the middle of both background and foreground regions. This can be explained by investigating the values of f_1 and f_2 at some points. For example, the values of f_1 and f_2 at three points p_1, p_2, and p_3 are shown in Fig. 2(b). For points p_1 and p_2, the values are equal to the intensities of the background and foreground respectively. As a result, the fitting energy $\mathcal{F}^{\mathrm{LBF}}$ at the points p_1, p_2 is minimized to zero, which results in the contour being stuck in the middle of both background and foreground regions. For the point p_3, the values of f_1 and f_2 approximate the local intensities on both sides of the contour very well. As a result, the local fitting energy $\mathcal{F}^{\mathrm{LBF}}$ is minimized, and therefore the contour is stopped at the object boundaries.

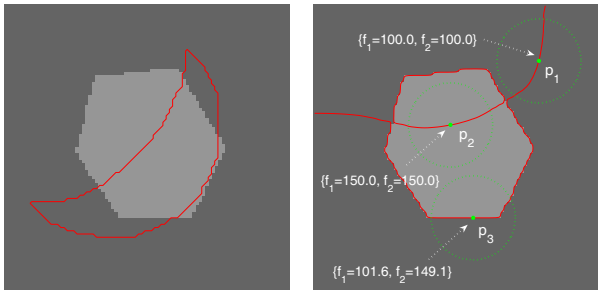

(a) (b)

Fig. 2. Result of the LBF model. (a) Original image and initial contour. (b) Final contour and values of $\{f_1, f_2\}$ for three points p_1, p_2, and p_3.

3 Method

Our method combines the advantages of the CV model and the LBF model by taking the local and global intensity information into account. In this section, we will detail our active contour model based on local and global intensity fitting (LGIF) for image segmentation.

3.1 Two-Phase Level Set Formulation

The local intensity fitting (LIF) energy [17] is defined as follows, which is the same as the first two terms in Eq. (2):

$$\begin{aligned}\mathcal{E}^{\mathrm{LIF}}(\phi, f_1, f_2) = \lambda_1 \int \Big[\int K_\sigma(\mathbf{x}-\mathbf{y}) |I(\mathbf{y}) - f_1(\mathbf{x})|^2 H(\phi(\mathbf{y})) d\mathbf{y} \Big] d\mathbf{x} \\ + \lambda_2 \int \Big[\int K_\sigma(\mathbf{x}-\mathbf{y}) |I(\mathbf{y}) - f_2(\mathbf{x})|^2 (1 - H(\phi(\mathbf{y}))) d\mathbf{y} \Big] d\mathbf{x} \quad (3)\end{aligned}$$

where ϕ is the level set function, $H(\cdot)$ is the Heaviside function [12].

We use the CV model's global intensity fitting (GIF) energy

$$\begin{aligned}\mathcal{E}^{\mathrm{GIF}}(\phi, c_1, c_2) = \lambda_1 \int |I(\mathbf{x}) - c_1|^2 H(\phi(\mathbf{x})) d\mathbf{x} \\ + \lambda_2 \int |I(\mathbf{x}) - c_2|^2 (1 - H(\phi(\mathbf{x}))) d\mathbf{x} \quad (4)\end{aligned}$$

Now, we define the following energy functional:

$$\mathcal{E}^{\mathrm{LGIF}}(\phi, f_1, f_2, c_1, c_2) = (1-\omega)\mathcal{E}^{\mathrm{LIF}}(\phi, f_1, f_2) + \omega \mathcal{E}^{\mathrm{GIF}}(\phi, c_1, c_2) \quad (5)$$

where ω is a positive constant ($0 \leq \omega \leq 1$). When the images are corrupted by intensity inhomogeneity, the parameter value ω should be chosen small enough. The selection of the parameter ω is discussed in Section 5.

For more accurate computation involving the level set function and its evolution, we need to regularize the level set function by penalizing its deviation from a signed distance function [6], which can be characterized by the following energy functional

$$\mathcal{P}(\phi) = \int_{\Omega} \frac{1}{2}(|\nabla\phi(\mathbf{x})| - 1)^2 d\mathbf{x} \tag{6}$$

As in typical level set methods [12,10], we need to regularize the zero level set by penalizing its length to derive a smooth contour during evolution:

$$\mathcal{L}(\phi) = \int_{\Omega} |\nabla H(\phi(\mathbf{x}))| d\mathbf{x} \tag{7}$$

Now, we define the entire energy functional

$$\mathcal{F}(\phi, f_1, f_2, c_1, c_2) = \mathcal{E}^{\mathrm{LGIF}}(\phi, c_1, c_2, f_1, f_2) + \nu\mathcal{L}(\phi) + \mu\mathcal{P}(\phi) \tag{8}$$

where $\nu > 0$ and $\mu > 0$ are constants as the weights of the term $\mathcal{L}(\phi)$ and the term $\mathcal{P}(\phi)$, respectively.

In practice, Heaviside function H is approximated by a smooth function H_ϵ defined by

$$H_\epsilon(\mathbf{x}) = \frac{1}{2}[1 + \frac{2}{\pi}\arctan(\frac{\mathbf{x}}{\epsilon})] \tag{9}$$

where ϵ is a positive constant. The derivative of H_ϵ is the smoothed Dirac delta function

$$\delta_\epsilon(\mathbf{x}) = H'_\epsilon(\mathbf{x}) = \frac{1}{\pi}\frac{\epsilon}{\epsilon^2 + \mathbf{x}^2} \tag{10}$$

The parameter ϵ in H_ϵ and δ_ϵ is set to 1.0 as in [12,10,17]. This parameter can

be fixed as this value in practice.

Thus, the energy functional $\mathcal{F}(\phi, f_1, f_2, c_1, c_2)$ in Eq. (8) is approximated by

$$\mathcal{F}_\epsilon(\phi, f_1, f_2, c_1, c_2) = \mathcal{E}_\epsilon^{\mathrm{LGIF}}(\phi, f_1, f_2, c_1, c_2) + \nu\mathcal{L}_\epsilon(\phi) + \mu\mathcal{P}(\phi) \tag{11}$$

We use the standard gradient descent (or steepest descent) method to minimize the energy functional (11). For a fixed level set function ϕ, we minimize the energy functional $\mathcal{F}_\epsilon(\phi, f_1, f_2, c_1, c_2)$ in Eq. (11) with respect to the functions $f_1(\mathbf{x})$, $f_2(\mathbf{x})$ and constants c_1, c_2. By calculus of variations, it can be shown that the functions $f_1(\mathbf{x})$, $f_2(\mathbf{x})$ and constants c_1, c_2 that minimize $\mathcal{F}_\epsilon(\phi, f_1, f_2, c_1, c_2)$ satisfy the following Euler-Lagrange equations:

$$\int K_\sigma(\mathbf{x}-\mathbf{y})(I(\mathbf{y}) - f_1(\mathbf{x}))H_\epsilon(\phi(\mathbf{y}))d\mathbf{y} = 0 \tag{12}$$

$$\int K_\sigma(\mathbf{x}-\mathbf{y})(I(\mathbf{y}) - f_2(\mathbf{x}))(1 - H_\epsilon(\phi(\mathbf{y})))d\mathbf{y} = 0 \tag{13}$$

$$\int (I(\mathbf{x}) - c_1)H_\epsilon(\phi(\mathbf{x}))d\mathbf{x} = 0 \tag{14}$$

$$\int (I(\mathbf{x}) - c_2)(1 - H_\epsilon(\phi(\mathbf{x})))d\mathbf{x} = 0 \tag{15}$$

From Eqs. (12) - (15), we obtain

$$f_1(\mathbf{x}) = \frac{K_\sigma(\mathbf{x}) * [H_\epsilon(\phi(\mathbf{x}))I(\mathbf{x})]}{K_\sigma(\mathbf{x}) * H_\epsilon(\phi(\mathbf{x}))} \tag{16}$$

$$f_2(\mathbf{x}) = \frac{K_\sigma(\mathbf{x}) * [(1 - H_\epsilon(\phi(\mathbf{x})))I(\mathbf{x})]}{K_\sigma(\mathbf{x}) * [1 - H_\epsilon(\phi(\mathbf{x}))]} \tag{17}$$

$$c_1 = \frac{\int I(\mathbf{x})H_\epsilon(\phi(\mathbf{x}))d\mathbf{x}}{\int H_\epsilon(\phi(\mathbf{x}))d\mathbf{x}} \tag{18}$$

$$c_2 = \frac{\int I(\mathbf{x})(1 - H_\epsilon(\phi(\mathbf{x})))d\mathbf{x}}{\int (1 - H_\epsilon(\phi(\mathbf{x})))d\mathbf{x}} \tag{19}$$

Minimization of the energy functional $\mathcal{F}_\epsilon(\phi, f_1, f_2, c_1, c_2)$ in Eq. (11) with respect to ϕ can be achieved by solving the gradient descent flow equation

$$\frac{\partial \phi}{\partial t} = \delta_\epsilon(\phi)(F_1 + F_2) + \nu\delta_\epsilon(\phi)\mathrm{div}\left(\frac{\nabla\phi}{|\nabla\phi|}\right) + \mu\left(\nabla^2\phi - \mathrm{div}\left(\frac{\nabla\phi}{|\nabla\phi|}\right)\right) \quad (20)$$

where

$$\begin{aligned} F_1 = (1-\omega)[-\lambda_1 \int K_\sigma(\mathbf{y}-\mathbf{x})|I(\mathbf{x}) - f_1(\mathbf{y})|^2 d\mathbf{y} \\ + \lambda_2 \int K_\sigma(\mathbf{y}-\mathbf{x})|I(\mathbf{x}) - f_2(\mathbf{y})|^2 d\mathbf{y}] \end{aligned} \quad (21)$$

and

$$F_2 = \omega[-\lambda_1|I(\mathbf{x}) - c_1|^2 + \lambda_2|I(\mathbf{x}) - c_2|^2] \quad (22)$$

We call F_1 and F_2 the local intensity fitting (LIF) force and global intensity fitting (GIF) force, respectively.

The influence of the LIF force and GIF force on the curve evolution is complementary. When the contour is near object boundaries, the LIF force is dominant, which attracts the contour toward object boundaries and finally stops the contour there. Therefore, the location of the final contour is determined by the LIF force. When the contour is far away from object boundaries, the GIF force is dominant, while the LIF force is close to zero. This can be illustrated by an example shown in Fig. 3. The initial contour and the contour after 10 iterations are plotted in yellow and green respectively. The blue and red arrows represent the LIF and GIF forces [2], respectively. It can be seen that

[2] According to the general relation between curve evolution and level set evolution [25,6], the direction of the LIF and GIF forces is $-\nabla\phi$ (see Appendix for detailed explanation).

the LIF force is dominant near the object boundaries, while the GIF force is dominant at locations far away from the object boundaries.

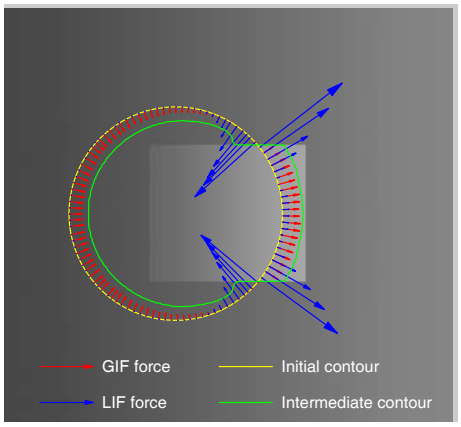

Fig. 3. Influence of LIF and GIF forces.

3.2 Extension to Multi-phase Level Set Formulation

The model proposed above is a two-phase level set formulation, which is not able to segment multiple regions that are adjacent to each other (a situation often referred to as multiple junctions). For example, in brain MR images, the regions of white matter (WM), gray matter (GM), and cerebrospinal fluid (CSF) may be adjacent to each other. In this section, we extend the LGIF model to a multi-phase level set formulation to segment multiple junctions. An important application of this multi-phase formulation is for the segmentation of WM, GM and CSF. In multi-phase level set formulation, n level set functions can represent 2^n regions [10]. The multi-layer level set formulation can also represent multiple regions [26]. In this paper, we focus on four-phase formulation, which is sufficiently to segment brain MR images. Two level set functions ϕ_1, ϕ_2 are used to define the partition of image domain into four disjoined regions [10]: $\{\phi_1 > 0, \phi_2 > 0\}$, $\{\phi_1 > 0, \phi_2 < 0\}$, $\{\phi_1 < 0, \phi_2 > 0\}$, $\{\phi_1 < 0, \phi_2 < 0\}$. We define the following energy functional,

$$
\begin{aligned}
&\mathcal{F}(\phi_1, \phi_2, f_1, f_2, f_3, f_4, c_1, c_2, c_3, c_4) \\
&= (1-\omega)\sum_{i=1}^{4}\lambda_i \int\int K_\sigma(\mathbf{x}-\mathbf{y})|I(\mathbf{y})-f_i(\mathbf{x})|^2 M_i(\mathbf{y})d\mathbf{y}d\mathbf{x} \\
&+ \omega\sum_{i=1}^{4}\lambda_i \int |I(\mathbf{x})-c_i|^2 M_i(\mathbf{x})d\mathbf{x} \\
&+ \nu(\mathcal{L}_\epsilon(\phi_1)+\mathcal{L}_\epsilon(\phi_2)) + \mu(\mathcal{P}(\phi_1)+\mathcal{P}(\phi_2))
\end{aligned} \tag{23}
$$

where $M_1 = H_\epsilon(\phi_1)H_\epsilon(\phi_2)$, $M_2 = H_\epsilon(\phi_1)(1-H_\epsilon(\phi_2))$, $M_3 = (1-H_\epsilon(\phi_1))H_\epsilon(\phi_2)$, $M_4 = (1-H_\epsilon(\phi_1))(1-H_\epsilon(\phi_2))$, and $\mathcal{L}_\epsilon(\phi_i) = \int |\nabla H_\epsilon(\phi_i(\mathbf{x})|d\mathbf{x}$, and $\mathcal{P}(\phi_i) = \int \frac{1}{2}(|\nabla\phi_i(\mathbf{x})|-1)^2 d\mathbf{x}$. We fix $\lambda_i = 1$ in our implementation for the multi-phase formulation of LGIF model. Therefore, we omit λ_i for simplicity of notation.

Minimizing Eq. (23), we obtain $f_1, \cdots, f_4, c_1, \cdots, c_4$ as follows:

$$
f_i(\mathbf{x}) = \frac{K_\sigma(\mathbf{x}) * [M_i I(\mathbf{x})]}{K_\sigma(\mathbf{x}) * M_i}, \quad c_i = \frac{\int I(\mathbf{x})M_i d\mathbf{x}}{\int M_i d\mathbf{x}}, \quad i = 1, \cdots, 4 \tag{24}
$$

Minimizing the energy functional $\mathcal{F}$ in Eq. (23) with respect to ϕ_1, we derive the gradient descent flow:

$$
\begin{aligned}
\frac{\partial\phi_1}{\partial t} &= \delta_\epsilon(\phi_1)\Big(F_{13}+F_{24}\Big) + \nu\delta_\epsilon(\phi_1)\mathrm{div}\left(\frac{\nabla\phi_1}{|\nabla\phi_1|}\right) \\
&\quad + \mu\left(\nabla^2\phi_1 - \mathrm{div}\left(\frac{\nabla\phi_1}{|\nabla\phi_1|}\right)\right)
\end{aligned} \tag{25}
$$

where

$$
F_{13} = H_\epsilon(\phi_2)(e_3 - e_1) \tag{26}
$$

$$
F_{24} = (1-H_\epsilon(\phi_2))(e_4 - e_2) \tag{27}
$$

and e_i is a function

$$
e_i(\mathbf{x}) = (1-\omega)\int K_\sigma(\mathbf{y}-\mathbf{x})|I(\mathbf{x})-f_i(\mathbf{y})|^2 d\mathbf{y} + \omega|I(\mathbf{x})-c_i|^2 \tag{28}
$$

Likewise, minimizing the energy functional $\mathcal{F}$ with respect to ϕ_2, we derive the gradient descent flow:

$$\frac{\partial \phi_2}{\partial t} = \delta_\epsilon(\phi_2)\Big(F_{12} + F_{34}\Big) + \nu\delta_\epsilon(\phi_2)\mathrm{div}\left(\frac{\nabla\phi_2}{|\nabla\phi_2|}\right) + \mu\left(\nabla^2\phi_2 - \mathrm{div}\left(\frac{\nabla\phi_2}{|\nabla\phi_2|}\right)\right) \tag{29}$$

where

$$F_{12} = H_\epsilon(\phi_1)(e_2 - e_1) \tag{30}$$

$$F_{34} = (1 - H_\epsilon(\phi_1))(e_4 - e_3) \tag{31}$$

4 Implementation and results

4.1 Two-phase segmentation

The level set function ϕ can be simply initialized as a binary step function [6] which takes a negative constant value $-c_0$ inside a region R_0 and a positive constant value c_0 outside. We choose $c_0 = 2$ in the experiments shown in this paper. The proposed method has been tested with synthetic and real images from different modalities. Unless otherwise specified, we use the following default setting of the parameters in our method: $\sigma = 3.0$, $\lambda_1 = \lambda_2 = 1.0$, time step $\triangle t = 0.1$, $\mu = 1.0$, $\omega = 0.01$, and $\nu = 0.001 \times 255 \times 255$.

We first apply our method to segment a synthetic image shown in Fig. 4. Note that this image is the same as Fig. 1 but with the initialization as shown in Fig. 4(a), which has shown that the LBF model fails to segment the object correctly with such initialization. The results of the CV model, LBF model

and our method are shown in Fig. 1(b), Fig. 4(b) and 4(c), respectively. It is clearly seen that the CV model cannot handle intensity inhomogeneity as explained in Section 2.1, and the LBF model got trapped into a local minimum without taking global image information into account. By contrast, our model, driven by the LIF and GIF forces, successfully extracts the object boundaries.

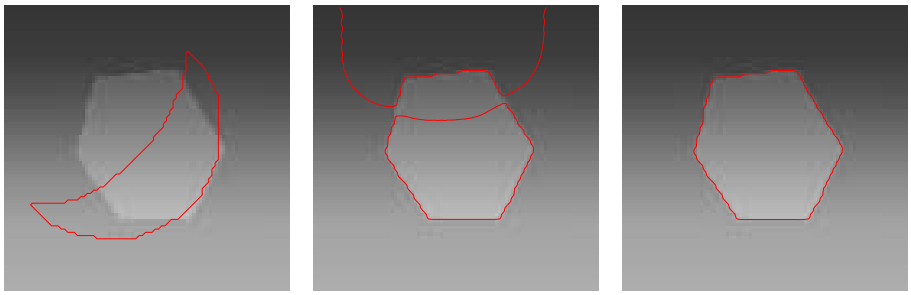

(a) (b) (c)

Fig. 4. Experiment for a synthetic image with intensity inhomogeneity. (a) Initial contour. (b) Result of the LBF model. (c) Result of our method.

Intensity inhomogeneity often occurs in medical images, such as the images shown in Fig. 5. All of them are typical images with intensity inhomogeneity. The first row shows the results for a vessel image. In this image, part of the vessel boundaries are quite weak, which renders it a nontrivial task to segment the vessel from the background. The second row shows the result for a brain MR image. As can be seen in this image, some intensities of the WM in the upper part are even lower than those of the GM in the lower part. For this image, we used the parameters $\lambda_1 = 1.0$, $\lambda_2 = 2.0$, and $\nu = 0.003 \times 255 \times 255$. The bottom row shows the result for a CT image of heart. The contour is placed across the interventricular septum of the heart. In next subsection, we show an example that the LBF model fails to extract ventricles with this initialization (see Fig. 6). Nevertheless, satisfactory segmentation results have

been obtained for these images, as shown in the last column of Fig. 5.

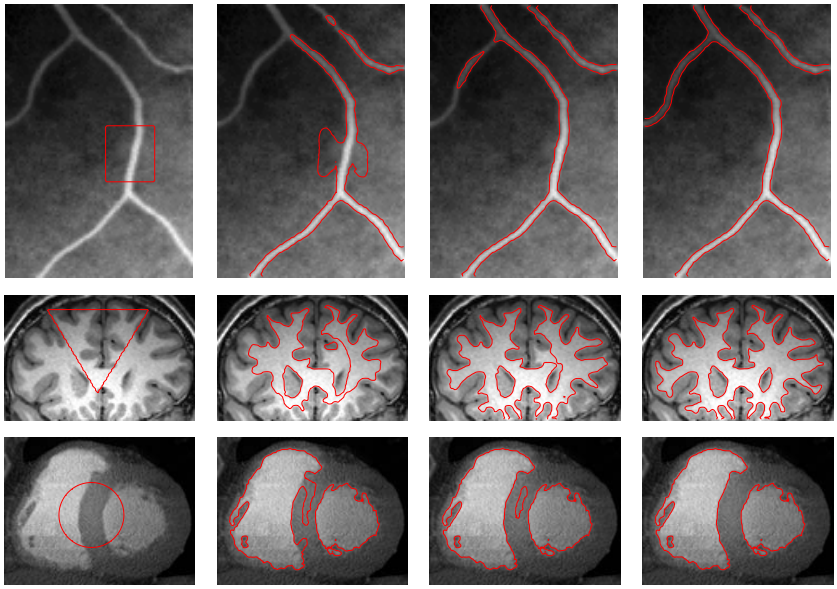

Fig. 5. Application to medical images. The curve evolution process from the initial contour (in the first column) to the final contour (in the fourth column) is shown in every row.

Since PS model is computationally expensive due to its complex procedure [18], we focus on the comparison of our model with the PC model [12] and the LBF model on the images shown in the Fig. 5. Fig. 6 shows the results of the PC model (the left column), the LBF model (the middle column) and our method (the right column). For the vessel image (the first row), our method and the LBF model have similar final results, while the PC model fails to extract the object boundaries. The second row shows the results on the brain MR image. It can be seen that small portions of the WM are missing. For the heart image (the third row), our method extracts the ventricle boundaries accurately, while the contour of the LBF model is somewhat noisy and finally fails to extract the object boundaries. With the same initializations, our method can achieve satisfactory results while other methods fail, which

demonstrates the advantage of our model in term of robustness to the initialization.

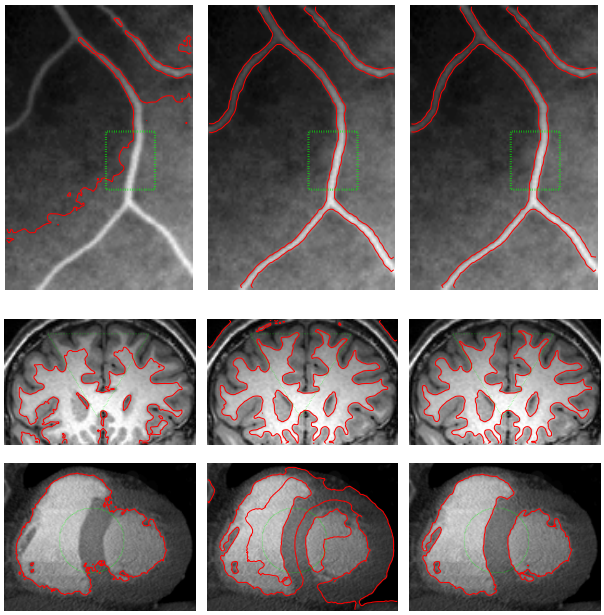

Fig. 6. Comparison of our method with the PC model and LBF model. The initial contours and the final contours are plotted as the dashed green contours and solid red contours, respectively. Column 1: Results of the PC model; Column 2: Results of the LBF model; Column 3: Results of our method.

4.2 Multi-phase segmentation of brain MR images

The segmentation of the brain MR images into WM, GM, and CSF has been an important task in medical image analysis. A major difficulty in segmentation of MR images is the intensity inhomogeneity due to the radio-frequency coils or acquisition sequences. Our method is able to address the difficulty. In this subsection, we will show an application of our multi-phase model to the segmentation of brain MR images.

We first apply our multi-phase model to segment a 2D MR image from McGill

Brain Web [27] with noise level 3%, and intensity non-uniformity (INU) 40% as shown in Fig. 7(a). We have increased INU to test the validity of our method to handle intensity inhomogeneity. In fact, the intensity of WM in the lower part is even lower than that of the GM in the upper part. The contours are initialized as two circles shown in Fig. 7(a). The curve evolution is depicted in the top row of Fig. 7. It can be observed that WM, GM, and CSF are well segmented by our method. Total number of iterations is 182.

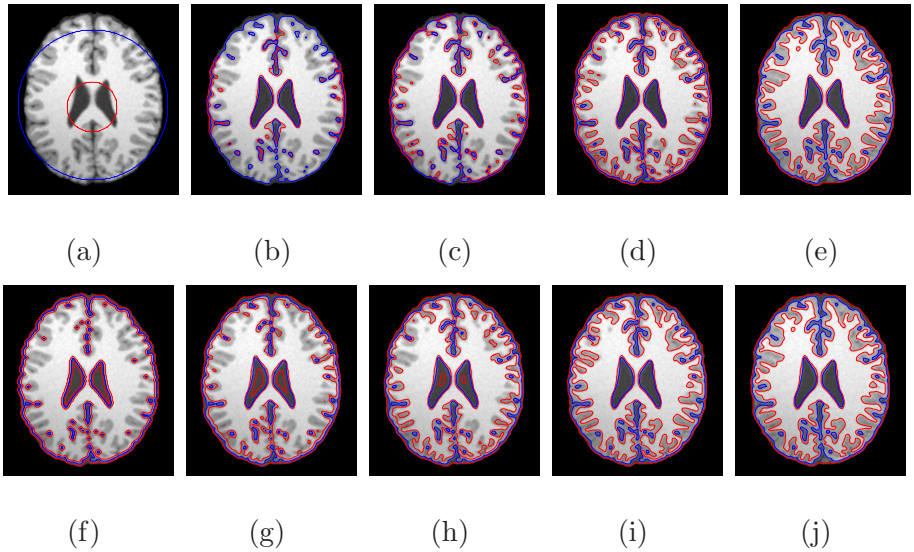

Fig. 7. Application to brain MR image segmentation. The red curve and blue curve are zero level sets of ϕ_1 and ϕ_2. (a) and (f): Initial contours. (b-e) and (g-j): Intermediate results of our method. Upper row: results with user interaction. Lower row: results with automatic initialization.

In practice, to reduce the number of iterations, we can initialize the contour close to the true boundaries by a preliminarily segmentation. In our implementation, we use a simple thresholding to obtain two regions: one as the preliminarily segmented region of background and CSF, the other as the preliminarily segmented region of GM and WM, denoted by R. Then, we perform the dilation and erosion operations to expand and shrink the region R, respectively. As a result, we obtain a expanded version of R, denoted by $R_{expanded}$,

and a shrunk version of R, denoted by R_{shrunk}. Following the initialization scheme in [28], the level set functions $\phi_{1,0}$ and $\phi_{2,0}$ are initialized as

$$\phi_{1,0}(\mathbf{x}) = \begin{cases} c_0, & if \quad \mathbf{x} \notin R; \\ -c_0, & else; \end{cases} \tag{32}$$

$$\phi_{2,0}(\mathbf{x}) = \begin{cases} c_0, & if \quad \mathbf{x} \notin R_{expanded} \quad or \quad \mathbf{x} \in R_{shrunk}; \\ -c_0, & else; \end{cases} \tag{33}$$

where c_0 is a constant. Then the contours are initialized near the boundaries of WM, GM and CSF. Thus, less iterations are needed to obtain the final segmentation result. For example, the lower row of Fig. 7 shows the results with the new initialization scheme. The initial contours are shown in Fig. 7(f). The curve evolution is depicted in the lower row. The final segmentation is similar with the one shown in the top row, but only 45 iterations are needed.

Note that new contours can emerge during the curve evolution shown in Fig. 7. The emergence of new contours speeds up the curve evolution toward final results. The emergence of new contours can be explained as follows. Note that the terms $\delta_\epsilon(\phi_1)\Big(F_{13} + F_{24}\Big)$ in Eq. (25) and $\delta_\epsilon(\phi_2)\Big(F_{12} + F_{34}\Big)$ in Eq. (29) have influence on the change of ϕ_1 and ϕ_2 in the entire image domain, since the factor δ_ϵ is non-zero by the definition of δ_ϵ in Eq. (10). For points $\mathbf{x}$ far away from the zero level contour but near an object boundary, the values of $\Big(F_{13} + F_{24}\Big)$ and $\Big(F_{12} + F_{34}\Big)$ may still be large. Although the factor δ_ϵ takes small values far away from the zero level set, the terms $\delta_\epsilon(\phi_1)\Big(F_{13} + F_{24}\Big)$ and $\delta_\epsilon(\phi_2)\Big(F_{12} + F_{34}\Big)$ are not zero and cannot be ignored, which can

eventually change the values of ϕ_1 and ϕ_2. When the level set functions ϕ_1 and ϕ_2 are initialized to be small values, such as the binary step function used in our implementation, new contours can emerge easily and quickly, even at locations far away from current zero level set. This is because the factor δ_ϵ takes relatively larger values for small values of ϕ_1 and ϕ_2 (in our experiments, the initial level set functions as binary step functions take values of c_0 and $-c_0$ with $c_0 = 2$).

Fig. 8 shows the surfaces of the GM and WM segmentation of real 3D brain MR images with obvious intensity inhomogeneity. The upper and lower row show the results obtained by the PC model [10] and our model, respectively. It can be seen that GM obtained by the PC model is a little bit thinner at the top of the brain and WM is seriously misclassified as GM. While the surfaces obtained by our method are more accurate. To demonstrate the advantage of our method clearly, we show four sagittal slices and the corresponding contours obtained by the PC model and our method in Fig. 9. It can be clearly seen that the PC model does not correctly segment images: part of the WM is incorrectly identified as the GM, while part of the GM is labeled as the WM. By contrast, our method recovers the boundaries of WM, GM, and CSF accurately.

4.3 Validation and Method Comparison

Fig. 10 shows the comparison of the proposed method with the methods of Wells *et al.* [29] and Leemput *et al.* [30] on five brain MR images. These two methods are based on expectation-maximization (EM) algorithm for interleaved bias field correction and segmentation. The first column shows the original images. The ground truth segmentation of the first image (the top-

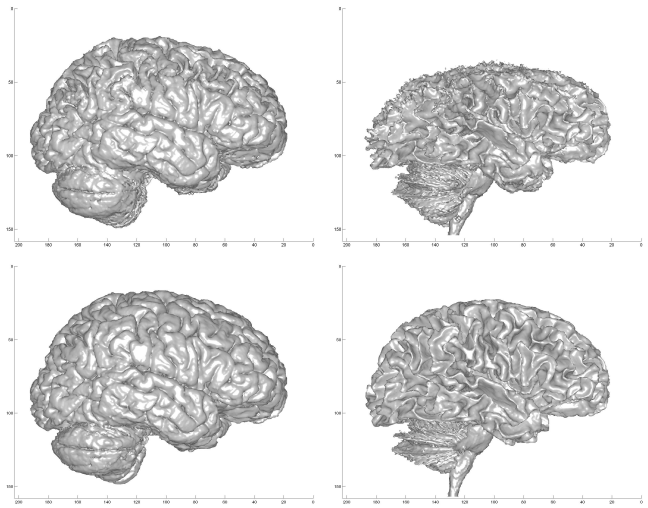

Fig. 8. Results for 3D brain MR images. Row 1: GM and WM surfaces obtained by the PC model; Row 2: GM and WM surfaces obtained by our model.

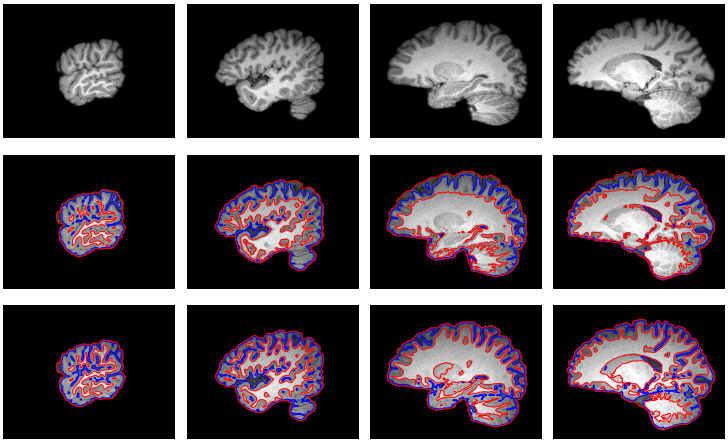

Fig. 9. Results of sagittal slices from 3D segmentation of Fig. 8. The red curve and blue curve are zero level sets of ϕ_1 and ϕ_2. Row 1: Original image slices; Row 2: Results of PC model; Row 3: Results of our method.

left) was obtained from Brain Web [27]. The other four images are real images and the corresponding ground truth of these images were obtained from expert manual segmentation, as shown in the second column. The segmentation results obtained by the methods of Wells *et al.* , Leemput *et al.* and the proposed method are shown in columns 3, 4 and 5, respectively. The segmentation results are visualized by displaying $\sum_{i=1}^{4} c_i M_i$. It can be observed that the re-

sults of our model and the methods of Wells *et al.* and Leemput *et al.* look similar by visual comparison. However, we can show by quantitative comparison that our model produces more accurate results. The metric adopted in this paper for comparison is the Dice Similarity Coefficient (DSC) [31], which is defined as

$$DSC = \frac{2N(S_1 \bigcap S_2)}{N(S_1) + N(S_2)} \tag{34}$$

where S_1 and S_2 represent the obtained segmentation and ground truth, respectively, and $N(\cdot)$ indicates the number of voxels in the enclosed set. The closer the DSC value to 1, the better the segmentation. Fig. 11 shows the DSC values for WM and GM of these methods. It can be seen that our method achieves more accurate results.

5 Discussion

5.1 The parameter ω

In this paper, the parameter ω is a constant, which controls the influence of the LIF force and GIF force. When the intensity inhomogeneity is severe, the accuracy of segmentation relies on the LIF force. In such case, we shall choose small ω as the weight of the GIF force; otherwise the GIF force may prevent the LIF force stopping at object boundaries. When the intensity inhomogeneity is not severe, for example, an extreme case of intensity homogeneity, we can choose large ω as the weight of the GIF force, due to the GIF force is sufficient to detect object boundaries, therefore, flexible initialization of the contour is allowed. In the experiment, we need to choose appropriate value for

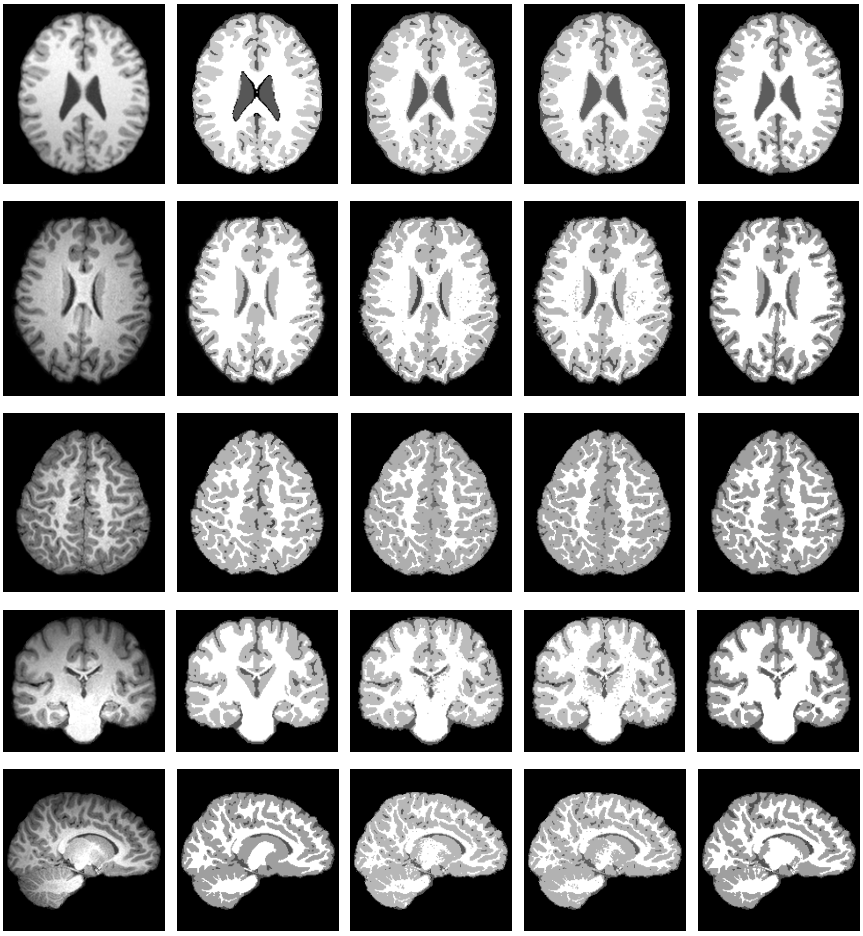

Fig. 10. Comparison of our method with the methods of Wells *et al.* , Leemput *et al.* on brain MR images. Column 1: Original images (The first image is the same as the image shown in Fig. 7. The other four images are real images); Column 2: Ground truth; Column 3: Wells *et al.* ; Column 4: Leemput *et al.* ; Column 5: Our method.

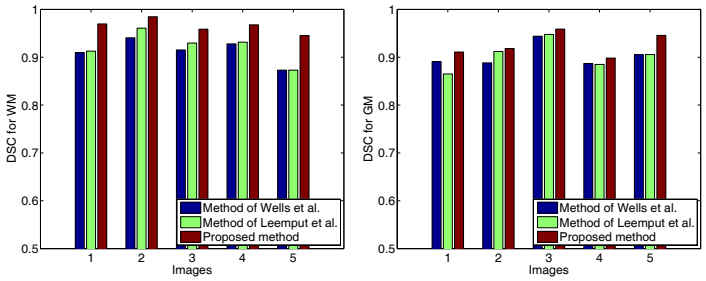

Fig. 11. DSC values for WM (left) and GM (right). The x-axis represents five images in Fig. 10 in the same order.

ω according to the degree of inhomogeneity. Fortunately, we find that $\omega = 0.01$ is appropriate for all the images in this paper.

5.2 Effect of level set regularization term

The level set regularization term $\mathcal{P}$ defined in (6) is necessary in the proposed variational level set formulation [3]. Without the level set regularization term (i.e., $\mu = 0$), the level set function ϕ typically grows to very large positive or negative values on both sides of the zero level set, resulting in arbitrarily large gradients there. This irregularity of ϕ causes errors in the computation for the numerical solution to the evolution equation and affects the accuracy of final segmentation results. Therefore, an extra numerical remedy, known as re-initialization, is usually required to periodically stop the evolution and reshape the degraded level set function as a signed distance function for further evolution and accurate computation. By contrast, the regularity of the level set function in our method is inherently maintained by the level set evolution itself due to the regularization mechanism of the level set regularization term.

Fig. 12 shows three experimental results for the MR image in Fig. 5 for the following three cases: a) with level regularization; b) without level set regularization, and re-initialization is not performed; c) without level set regularization but re-initialization is performed. Note that the initial contour is the same as shown in Fig. 5. For comparison, we show the segmentation results and the final level set functions for this figure. For the case a), it can be clearly seen

[3] The level set regularization term can be defined as $\mathcal{P} = \int p(|\nabla\phi(\mathbf{x})|)d\mathbf{x}$, where p is a function. For example, we can choose $\mathcal{P} = \int (|\nabla\phi(\mathbf{x})|-1)^2 d\mathbf{x}$ or $\mathcal{P} = \int |\nabla\phi(\mathbf{x})|^2 d\mathbf{x}$. More general level set regularization term is proposed by Li *et al.* in [28]

from the result in Fig. 12(d) that the regularity of ϕ is well preserved, and the segmentation result is desirable. For the case b) (the second column), the irregularity of ϕ affects the accuracy in the segmentation and creates some unwanted noisy features as shown in Fig. 12(e). For the case c) (the third column), the regularity of ϕ is preserved, however, the segmentation result is inaccurate, which can be clearly seen in Fig. 12(c).

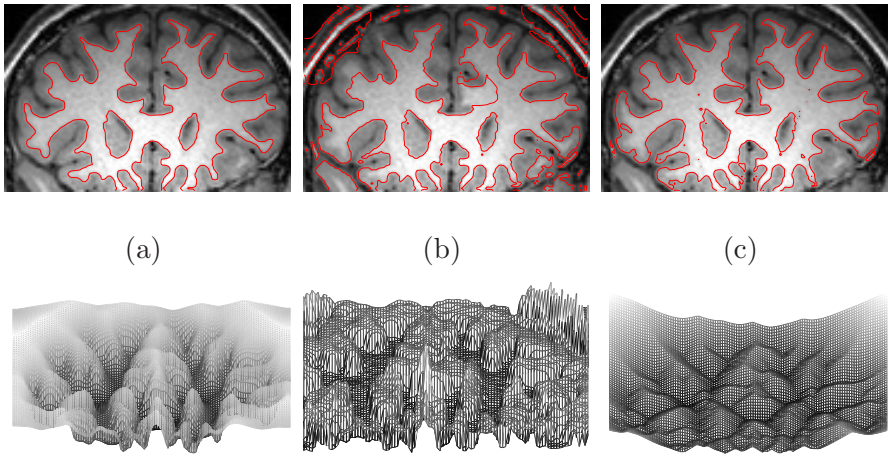

(a) (b) (c)

(d) (e) (f)

Fig. 12. Effect of level set regularization. (a) and (d) Segmentation result and final level set function ϕ with level set regularization. (b) and (e) Segmentation result and final level set function ϕ without level set regularization, and without re-initialization. (c) and (f) Segmentation result and final level set function ϕ without level set regularization, but with re-initialization.

We also test our multi-phase model for the cases a), b), and c) as shown in Fig. 13. It is evidently that the segmentation result of our method with level set regularization is desirable as shown in Fig. 13(a). The result is quite consistent with the brain anatomy. In contrast, for the cases b) and c), the results (Figs. 13(b) and 13(c)) are not consistent with the anatomy of brain in some areas, such as those pointed by the dashed green arrows. For example, WM is mislabeled as GM in those areas.

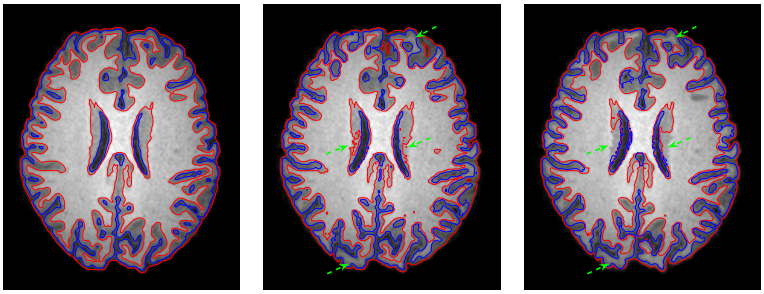

(a) (b) (c)

Fig. 13. Effect of level set regularization. (a) Result with level set regularization. (b) Result without level set regularization, and without re-initialization. (c) Result without level set regularization, but with re-initialization.

6 Conclusion

In this paper, we propose a new region-based active contour model in a variational level set formulation. We define an energy functional with a local intensity fitting term, which is dominant near object boundaries and responsible for attracting the contour toward object boundaries, and an auxiliary global intensity fitting term, which incorporates global image information to improve the robustness of the proposed method. Our model can handle intensity inhomogeneity, and allows for flexible initialization. In addition, the regularity of the level set function is intrinsically preserved by the level set regularization term to ensure accurate computation and thus avoid expensive reinitialization procedures. We further extend our two-phase LGIF model into a multi-phase level set formulation. Experimental results demonstrate desirable performance of our extension method for brain MR images with intensity inhomogeneity.

Appendix

The level set method is a numerical technique for tracking interfaces and shapes. The motion of the interfaces can be described by an curve evolution equation of a parameterized curve $\mathcal{C}$ in the form

$$\frac{\partial \mathcal{C}}{\partial t} = F\mathcal{N} \tag{35}$$

where F is the *speed function*, and $\mathcal{N}$ is the inward normal vector to the curve $\mathcal{C}$. The basic idea of the level set method is to embed the dynamic curve $\mathcal{C}(p,t)$ as the zero level set of a time dependent function $\phi(x,y,t)$, and then convert the curve evolution in Eq. (35) to the evolution of the embedding level set function ϕ. If the embedding level set function ϕ takes negative values inside the zero level contour and positive values outside, then the inward normal vector can be expressed as $\mathcal{N} = -\frac{\nabla\phi}{|\nabla\phi|}$. By simple calculus manipulations, the curve evolution equation (35) can then be converted to the following level set evolution equation

$$\frac{\partial \phi}{\partial t} = F|\nabla\phi| \tag{36}$$

which is a Hamilton-Jacobi equation.

Acknowledgements

The authors would like to thank X. Hong and C. He for providing their hand segmentation results, and the anonymous reviewers for their supportive and constructive comments. L. Wang, Q. Sun, and D. Xia acknowledge the support

from National Natural Science Funds. C. Li would like to thank the support from Vanderbilt University Institute of Imaging Science. C-Y. Kao acknowledges the support and hosting from Mathematical Biosciences Institute at The Ohio State University.

Conflict of Interest Statement. None declared.

References

[1] M. Kass, A. Witkin, D. Terzopoulos, Snakes: active contour models, Int'l J. Comp. Vis. 1 (4) (1987) 321–331.

[2] V. Caselles, F. Catte, T. Coll, F. Dibos, A geometric model for active contours in image processing, Numer. Math. 66 (1) (1993) 1–31.

[3] R. Kimmel, A. Amir, A. Bruckstein, Finding shortest paths on surfaces using level set propagation, IEEE Trans. Patt. Anal. Mach. Intell. 17 (6) (1995) 635–640.

[4] R. Malladi, J. A. Sethian, B. C. Vemuri, Shape modeling with front propagation: a level set approach, IEEE Trans. Patt. Anal. Mach. Intell. 17 (2) (1995) 158–175.

[5] C. Xu, J. Prince, Snakes, shapes, and gradient vector flow, IEEE Trans. Imag. Proc. 7 (3) (1998) 359–369.

[6] C. Li, C. Xu, C. Gui, M. D. Fox, Level set evolution without re-initialization: A new variational formulation, in: Proceedings of IEEE Conference on Computer Vision and Pattern Recognition (CVPR), Vol. 1, 2005, pp. 430–436.

[7] C. Li, J. Liu, M. D. Fox, Segmentation of edge preserving gradient vector flow: An approach toward automatically initializing and splitting of snakes, in:

Proceedings of IEEE Conference on Computer Vision and Pattern Recognition (CVPR), Vol. 1, 2005, pp. 162–167.

[8] R. Ronfard, Region-based strategies for active contour models, Int'l J. Comp. Vis. 13 (2) (1994) 229–251.

[9] C. Samson, L. Blanc-Feraud, G. Aubert, J. Zerubia, A variational model for image classification and restoration, IEEE Trans. Patt. Anal. Mach. Intell. 22 (5) (2000) 460–472.

[10] L. Vese, T. Chan, A multiphase level set framework for image segmentation using the Mumford and Shah model, Int'l J. Comp. Vis. 50 (3) (2002) 271–293.

[11] A. Tsai, A. Yezzi, A. S. Willsky, Curve evolution implementation of the Mumford-Shah functional for image segmentation, denoising, interpolation, and magnification, IEEE Trans. Imag. Proc. 10 (8) (2001) 1169–1186.

[12] T. Chan, L. Vese, Active contours without edges, IEEE Trans. Imag. Proc. 10 (2) (2001) 266–277.

[13] N. Paragios, R. Deriche, Geodesic active regions and level set methods for supervised texture segmentation, Int'l J. Comp. Vis. 46 (3) (2002) 223–247.

[14] M. Rousson, R. Deriche, A variational framework for active and adaptative segmentation of vector valued images, in: MOTION '02: Proceedings of the Workshop on Motion and Video Computing, IEEE Computer Society, Washington, DC, USA, 2002, pp. 56–61.

[15] M. Rousson, D. Cremers, Implicit active shape models for 3d segmentation in mr imaging, in: International Conference on Medical Image Computing and Computer Assisted Intervention (1), 2004, pp. 209–216.

[16] D. Cremers, M. Rousson, R. Deriche, A review of statistical approaches to level set segmentation: Integrating color, texture, motion and shape, Int'l J. Comp. Vis. 72 (2) (2007) 195–215.

[17] C. Li, C. Kao, J. Gore, Z. Ding, Implicit active contours driven by local binary fitting energy, in: Proceedings of IEEE Conference on Computer Vision and Pattern Recognition (CVPR), IEEE Computer Society, Washington, DC, USA, 2007, pp. 1–7.

[18] J. Piovano, M. Rousson, T. Papadopoulo, Efficient segmentation of piecewise smooth images, in: SSVM07, Ischia, Italy, 2007, pp. 709–720.

[19] S. Awate, T. Tasdizen, N. Foster, R. Whitaker, Adaptive markov modeling for mutual-information-based, unsupervised MRI brain-tissue classification, Medical Image Analysis 10 (5) (2007) 726–739.

[20] W. Wong, A. Chung, Bayesian image segmentation using local iso-intensity structural orientation, IEEE Trans. Imag. Proc., 14 (10) (2005) 1512–1523.

[21] C. Li, C. Kao, J. C. Gore, Z. Ding, Minimization of region-scalable fitting energy for image segmentation, IEEE Trans. Imag. Proc. 17 (10) (2008) 1940–1949.

[22] T. Brox, D. Cremers, On the statistical interpretation of the piecewise smooth Mumford-Shah functional, in: SSVM07, Ischia, Italy, 2007, pp. 203–213.

[23] L. Wang, C. Li, Q. Sun, D. Xia, C. Kao, Brain MR image segmentation using local and global intensity fitting active contours/surfaces, in: Proceedings of Medical Image Computing and Computer Aided Intervention (MICCAI), Vol. LNCS 5241, Part I, 2008, pp. 384–392.

[24] D. Mumford, J. Shah, Optimal approximations by piecewise smooth functions and associated variational problems, Commun. Pure Appl. Math. 42 (5) (1989) 577–685.

[25] S. Osher, J. Sethian, Fronts propagating with curvature-dependent speed: algorithms based on Hamilton-Jacobi formulations, J. Comp. Phys. 79 (1) (1988) 12–49.

[26] G. Chung, L. Vese, Image segmentation using a multilayer level-set approach, Computing and Visualization in Science.

[27] http://www.bic.mni.mcgill.ca/brainweb/.

[28] C. Li, C. Xu, C. Gui, M. D. Fox, Distance regularized level set evolution and applications to image segmentation, to appear in IEEE Trans. Imag. Proc.

[29] W. Wells, E. Grimson, R. Kikinis, F. Jolesz, Adaptive segmentation of MRI data, IEEE Trans. Med. Imag. 15 (4) (1996) 429–442.

[30] V. Leemput, K. Maes, D. Vandermeulen, P. Suetens, Automated model-based bias field correction of MR images of the brain, IEEE Trans. Med. Imag. 18 (10) (1999) 885–896.

[31] D. W. Shattuck, S. R. Sandor-Leahy, K. A. Schaper, D. A. Rottenberg, R. M. Leahy, Magnetic resonance image tissue classification using a partial volume model, Neuroimage 13 (2001) 856–C876.